Journal of the Iranian Chemical Society
https://doi.org/10.1007/s13738-021-02237-5

ORIGINAL PAPER

A chiral (1*R*,2*R*)-*N*,*N*′-*bis*-(salicylidene)-1,2-diphenyl-1,2-ethanediamine Schiff base dye: synthesis, crystal structure, Hirshfeld surface analysis, computational study, photophysical properties and in silico antifungal activity

Alexey A. Shiryaev[1,2] · Anastasiya N. Goncharenko[1] · Tatyana M. Burkhanova[1,3] · Larisa E. Alkhimova[1] · Maria G. Babashkina[4] · Ravikumar Chandrasekaran[5] · Damir A. Safin[1,2,3]

Received: 16 December 2020 / Accepted: 5 March 2021

Abstract
We report synthesis, structural and computational studies, and photophysical properties of a chiral (1*R*,2*R*)-*N*,*N*′-*bis*-(salicylidene)-1,2-diphenyl-1,2-ethanediamine Schiff base dye (**1**). The structure of **1** was found to be in the enol-imine tautomer, stabilized by two intramolecular O–H···N hydrogen bonds. Molecules are packed into a 1D supramolecular chain through intermolecular C–H···O interactions. 1D chains are interlinked through intermolecular C–H···π intercations. As a result of intermolecular interactions, molecules of **1** are packed into a 3D supramolecular framework, yielding a **pcu alpha-Po primitive cubic; 6/4/c1; sqc1** topology defined by the point symbol of ($4^{12}\cdot6^3$). Favoured intermolecular H···H, H···C and H···O contacts are responsible for the overall crystal packing of the dye. Energy frameworks have been calculated to additionally analyse the overall crystal packing of **1**. The absorption spectra of **1** in THF, CH_2Cl_2 and CH_3CN each exhibit three intense bands in the UV region. The absorption spectra of **1** in EtOH, *n*PrOH, *i*PrOH and *n*BuOH, besides the same three intense bands in the UV region, contain an additional band in the visible region centred at about 410 nm, corresponding to the *cis*-keto-enamine tautomer. The absorption spectrum of **1** in MeOH contains an additional intense shoulder at about 350 nm. The emission spectrum of **1** in MeOH contains a broad band at 438 nm, arising from the emission of the enol-imine* form. Theoretical calculations based on density functional theory (DFT) were performed to verify the structure of **1** as well as its electronic and optical properties. The global chemical reactivity descriptors were estimated from the energy of the HOMO and LUMO orbitals. Molecular docking studies were performed to evaluate the antifungal activity of **1** against cytochrome P450 14 alpha-sterol demethylase (CYP51).

Keywords *N*-salicylidene aniline dye · Crystal structure · Hirshfeld surface analysis · Optical properties · Molecular docking · DFT

✉ Damir A. Safin
damir.a.safin@gmail.com

[1] University of Tyumen, Volodarskogo Str. 6, Tyumen, Russian Federation 625003

[2] Innovation Center for Chemical and Pharmaceutical Technologies, Ural Federal University named after the First President of Russia B.N. Eltsin, Mira Str. 19, Ekaterinburg, Russian Federation 620002

[3] Kurgan State University, Sovetskaya Str. 63/4, Kurgan, Russian Federation 640020

[4] Institute of Condensed Matter and Nanosciences, Université Catholique de Louvain, Place L. Pasteur 1, 1348 Louvain-la-Neuve, Belgium

[5] Thanthai Periyar EVR Government Polytechnic College, Vellore, Tamilnadu 632002, India

Published online: 09 April 2021

Introduction

Schiff bases $R^1R^2C=NR^3$ ($R^3 \neq H$), named after famous chemist Hugo Schiff, who discovered this type of compounds [1] are a condensation product of primary amine and ketone, yielding secondary ketimines $R^1R^2C=NR^3$ ($R^3 \neq H$), or aldehyde, yielding secondary aldimines $R^1R^2C=NR^3$ (R^1 or $R^2=H$, $R^3 \neq H$). The latter imines are commonly referred to as azomethines. Of Schiff bases, different families can be highlighted. Particularly, Schiff bases $R^1R^2C=NR^3$, where R^3 = phenyl or substituted phenyl (*N*-phenyl imines), are called anils [2, 3]. The other famous family of Schiff bases is *bis*-compounds referred to as salen-type compounds. The term "salen" refers to a tetradentate Schiff base, derived from salicylaldehyde and ethylenediamine, namely *N*,*N*′-ethylenebis(salicylimine). In general, the salen-type Schiff bases are the product of condensation of a diamine with two equivalents of a salicylaldehyde derivative. Metal complexes of the salen-type ligands are of great importance in many fields of practical application. For instance, a coordination complex of Co^{II} with salen, namely *N*,*N*′-*bis*-(salicylidene) ethylenediaminocobalt(II) (salcomine), as well as its derivatives are known as efficient carriers for O_2, oxidation catalysts and enzyme mimics [4–8]. Furthermore, a coordination compound of Mn^{III} with a chiral bulky salen-type ligand, namely *N*,*N*′-*bis*-(3,5-di-tert-butylsalicylidene)-1,2-cyclohexanediaminomanganese(III) chloride, is an efficient asymmetric catalyst in the Jacobsen epoxidation [9, 10]. A methyl-substituted salen derivative, namely *N*,*N*′-1,2-propylenebis(salicylimine) (salpn), is known as a metal deactivation additive in motor oils and motor fuels [11].

On the other hand, chirality is an important phenomenon in the nature [12–14]. Chiral Schiff bases as well as their metal complexes are of great importance for many practical applications, e.g. catalysis [4–11]. Of chiral Schiff bases, chiral salen-type compounds play a pivotal role [4–11]. Obviously, in this type of compounds, chirality can be generated either through the diamine or the phenyl fragments, or both. For example, chiral (*S*,*S*) and (*R*,*R*) 1,2-diaminocyclohexane or 1,2-diphenyl-1,2-ethanediamine are facile and efficient transmitters of chirality. Thus, being the most widely used chiral diamine precursors.

Schiff bases obtained from salicylaldehyde derivatives is an outstanding family due to the *ortho*-situated OH group, which is responsible for the possible tautomerization between the enol-imine and keto-enamine isomers, of which the latter one can adopt either the *cis*- or *trans*-isomers (Scheme 1) [15–24]. This type of Schiff bases are known for their rich colour pallete (from colourless through yellow to red) as a result of different isomeric forms (Scheme 1). Furthermore, colours can efficiently be induced by different stimuli, e.g. temperature, pH, solvent, etc. The distinctive feature of the salicylaldehyde-derived Schiff bases is an intramolecular O–H···N hydrogen bond, which is a characteristic for the enol-imine isomer, while the *cis*-keto-enamine form is characterized by the intramolecular N–H···O hydrogen bond (Scheme 1). The position of this volatile proton is dictated not only by substituents (R^1 and R^2, respectively; Scheme 1) but also, e.g., by the solvent nature.

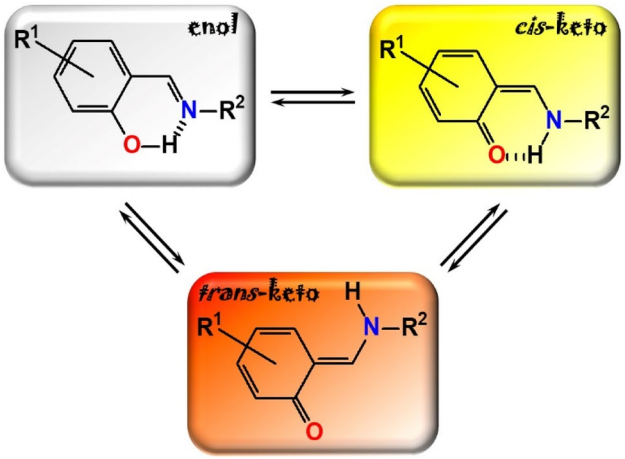

Scheme 1. Isomeric forms of *N*-salicylidene aniline derivatives and their colour panel

We also have extensively studied chromic properties of the salicylaldehyde derived Schiff bases [25–35]. In this work, we have directed our attention to a chiral (1*R*,2*R*)-*N*,*N*′-bis(salicylidene)-1,2-diphenyl-1,2-ethanediamine (**1**) Schiff base dye. We focused on optical properties of this compound in different solvents as well as we studied its crystal structure in details using Hirshfeld surface analysis. Furthermore, energy frameworks have been calculated to analyse the overall crystal packing of **1**. Using in silico molecular docking method, antifungal activity of **1** was also investigated against Cytochrome P450 14 alpha-sterol demethylase (CYP51) (PDB ID: 1EA1) antifungal enzyme.

Experimental

Physical measurements

The ATR-FTIR spectrum was recorded with a Nicolet iS20 FTIR spectrometer, while the FTIR spectrum in the KBr pellet was recorded with a JASCO-680 spectrometer. UV–vis and fluorescent spectra from the freshly prepared solutions in freshly distilled solvent were recorded on an Agilent 8453

instrument and a RF-5301PC Shimadzu spectrofluorometer, respectively. Elemental analysis was performed on a Thermo Flash 2000 CHNS analyser.

Synthesis

A mixture of salicylaldehyde (10 mmol, 1.221 g) and (1*R*,2*R*)-1,2-diphenyl-1,2-ethanediamine (5 mmol, 1.061 g) in ethanol (20 mL) was stirred at reflux for 1 h. The resulting hot solution allowed to cool to room temperature to give yellow block-like crystals of **1**. Yield: 1.640 g (78%). M. p.: 110–112 °C. *Anal.* Calc. for $C_{28}H_{24}N_2O_2$ (420.51): C 79.98, H 5.75 and N 6.66; found: C 80.11, H 5.67 and N 6.74%.

Computational details

The ground state geometry of **1** was fully optimized without symmetry restrictions. The calculations were performed by means of the GaussView 6.0 molecular visualization program [36] and Gaussian 09, Revision D.01 program package [37] using the density functional theory (DFT) with the hybrid with Becke-3-Lee–Yang–Parr (B3LYP) functional [38, 39] and 6–311 ++ G(d,p) [38, 40] basis set. The crystal structure geometry was used as a starting model for structural optimization. The vibration frequencies were calculated for the optimized structure in gas phase and no imaginary frequencies were obtained.

X-Ray powder diffraction

X-ray powder diffraction for a bulk sample was carried out using a Rigaku Ultima IV X-ray powder diffractometer. The Parallel Beam mode was used to collect the data (λ = 1.54184 Å).

Single crystal X-ray diffraction [41, 42]

Crystal data

$C_{28}H_{24}N_2O_2$, $M_r = 420.49$ g mol^{-1}, orthorhombic, space group $P2_12_12$, $a = 10.2076(6)$, $b = 16.3507(10)$, $c = 6.9936(4)$ Å, $V = 1167.24(12)$ Å^3, $Z = 2$, $\rho = 1.196$ g cm^{-3}, μ(Mo-Kα) = 0.076 mm^{-1}, $T = 296(2)$ K, reflections: 6613 collected, 2068 unique, $R_{int} = 0.122$, R_1(all) = 0.0399, wR_2(all) = 0.0979, $S = 1.079$.

CCDC 970499 contains the supplementary crystallographic data. These data can be obtained free of charge via http://www.ccdc.cam.ac.uk/conts/retrieving.html, or from the Cambridge Crystallographic Data Centre, 12 Union Road, Cambridge CB2 1EZ, UK; fax: (+44) 1223–336-033; or e-mail: deposit@ccdc.cam.ac.uk.

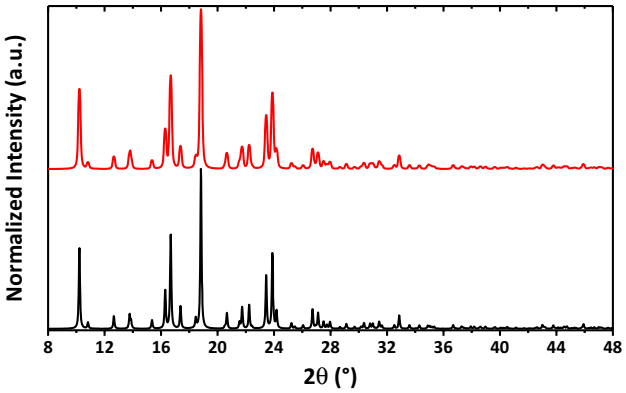

Fig. 1 Calculated (black) and experimental (red) X-ray powder diffraction patterns of **1**

Results and discussion

The dye **1** was obtained by the condensation reaction of (1*R*,2*R*)-1,2-diphenyl-1,2-ethanediamine with salicylaldehyde in ethanol (Scheme 2), yielding yellow X-ray suitable block-like crystals, which are stable under ambient conditions. A number of these crystals were tested by single-crystal X-ray diffraction, testifying to their identity and the obtained crystallographic parameters are the same as for the crystal structure of **1** found in the Cambridge Structural Database (CCDC number 970499) [41, 42]. The corresponding CIF file was subtracted from the CSD for an in-depth analysis (vide infra) of the crystal structure of **1**. Furthermore, the bulk sample of **1** is free from phase impurities as evidenced from comparison of the experimental X-ray

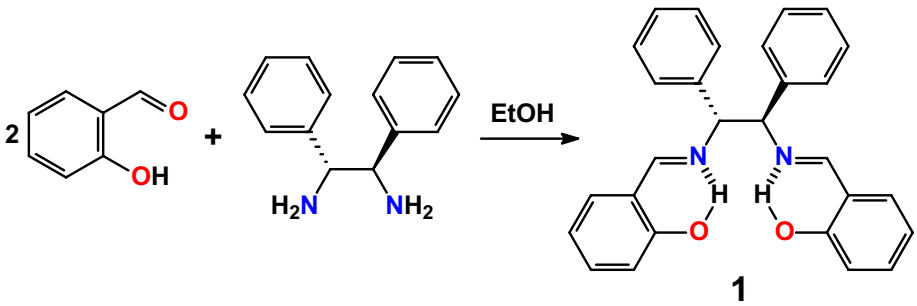

Scheme 2. Synthesis of the Schiff base dye **1**

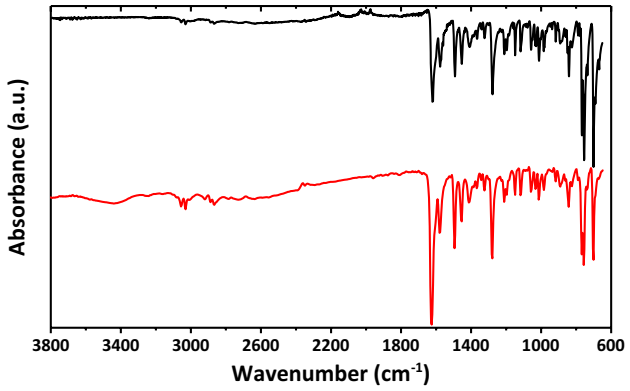

Fig. 2 ATR-FTIR spectrum (black) and FTIR spectrum, measured in the KBr pellet (red), of **1**

powder pattern with the calculated powder pattern generated from the single-crystal X-ray data (Fig. 1).

Compound **1** was characterized by the means of both ATR-FTIR spectroscopy and FTIR spectroscopy in the KBr pellet. Both spectra are the same in the fingerprint region except that in the ATR-FTIR spectrum the most intense bands were found at 701, 755 and 767 cm^{-1}, while in the FTIR spectrum recorded in the KBr pellet the most intense band was observed at 1625 cm^{-1} (Fig. 2). The former three bands were assigned as the C–H bending (our-of-plane) and ring torsion vibrations of the aromatic fragments, while the latter band was assigned as the ν(C=N) stretching, strongly supporting the formation of the imine function upon condensation of the parent diamine with salicylaldehyde. Aromatic rings are further reflected in the FTIR spectra of **1** as a band at 1580 cm^{-1}, corresponding to the C=C stretching vibrations. Another intense band at 1278 cm^{-1} corresponds to the C–O stretching. Notably, no bands characteristic for the NH_2 groups were observed in the FTIR spectra of **1** (Fig. 2), indicating the formation of the bifunctional Schiff base. The most crucial difference between two spectra is the presence of broad low intense, although visible, band centred at about 3440 cm^{-1} in the spectrum measured in the KBr pellet, while the same band was not observed in the ATR-FTIR spectrum (Fig. 2).

According to single-crystal X-ray diffraction, **1** crystallizes in the orthorhombic space group $P2_12_12$. The molecule lies on a crystallographic twofold axis; thus, the asymmetric unit comprises one half-molecule (Fig. 3). The C7–N1 bond length in the structure of **1** is 1.2650(18) Å, while the C8–N1 and C6–C7 bonds are similar and much longer and of 1.4537(16) and 1.448(2) Å, respectively (Table 1). The C1–O1 and C1–C6 bonds are 1.3474(19) and 1.4048(19) Å, respectively. Thus, all the discussed above bond lengths strongly suggest the formation of an enol-imine isomer of **1** in the solid state (Fig. 3) [43–46]. The C7–N1–C8 and C6–C7–N1 bond angles are very similar and of 119.92(11) and 122.68(12)°, respectively, indicating the sp^2-hybridization of both the carbon and the nitrogen atoms of the C7–N1 fragment in the structure of **1**. The overall X-shape of a molecule of **1** is dictated by the corresponding dihedral angles between the least-square planes formed by the phenylene and phenyl rings, which vary from 28.5° to 63.14(9)° (Table 1).

The crystal structure of **1** is stabilized by intramolecular O–H···N hydrogen bonds (Fig. 3, Table 2), yielding two six-membered hydrogen bonded heterocycles, which are almost perfectly planar as evidenced from the corresponding dihedral angles (Table 1).

The structure of **1** is further stabilized by intermolecular C–H···O interactions (Table 2), formed by one of the *ortho*-hydrogen atoms of the phenyl fragments and the hydroxyl oxygen atoms, yielding a 1D supramolecular chain, comprising $R^2_2(20)$ H-bonded cycles (Fig. 4). These 1D chains are further interlinked through intermolecular C–H···π intercations (Table 2), formed by one of the hydrogen atoms of the phenylene fragments and the π-system of the phenyl rings (Fig. 4). As a result of intermolecular interactions, molecules of **1** are packed into a 3D supramolecular framework (Fig. 4). This 3D supramolecular framework was simplified, using the ToposPro software [47], resulting in a **pcu alpha-Po primitive cubic; 6/4/c1; sqc1** topology defined by the point symbol of $(4^{12}\cdot6^3)$ (Fig. 4).

Crystal packing of **1** was further studied by a Hirshfeld surface analysis [48], also reflected in a set of corresponding 2D fingerprint plots [49], which were generated using CrystalExplorer 17 [50]. Additionally, the enrichment ratios (*E*) [51] of the intermolecular contacts were also calculated to estimate the propensity of two chemical species to be in contact.

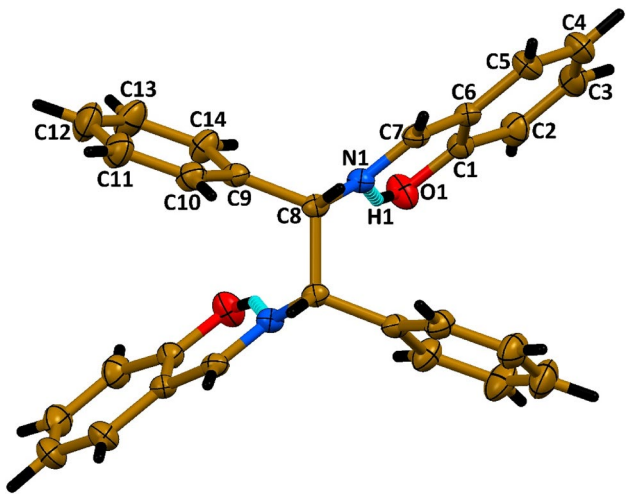

Fig. 3 Crystal structure of **1**. Colour code: H = black, C = gold, N = blue, O = red; O–H···N hydrogen bond = dashed cyan line

Table 1 Selected bond lengths (Å) and angles (°) in the structure of **1**.[a]

	Experimental	DFT (B3LYP/6–311 + + G(d,p))
Bond lengths		
C7–N1	1.2650(18)	1.2822
C8–N1	1.4537(16)	1.4526
C1–O1	1.3474(19)	1.3417
C1–C6	1.4048(19)	1.4183
C6–C7	1.448(2)	1.4538
Bond angles		
C7–N1–C8	119.92(11)	118.45
C6–C7–N1	122.68(12)	123.06
Dihedral angles		
H1–O1–C1–C6	−5	−0.2
O1–C1–C6–C7	5.2(2)	0.1
C1–C6–C7–N1	−3.1(2)	−0.5
C6–C7–N1···H1	0.7	0.6
C7–N1···H1–O1	−0.7	−1.0
N1···H1–O1–C1	3	0.7
C6–C7–N1–C8	173.78(12)	179.74
C7–N1–C8–C8_a	−124.69(13)	−116.68
C7–N1–C8–C9	112.61(13)	118.36
$Cg_{phenylene}\cdots Cg_{phenylene\_a}$[b]	34.7	4.0
$Cg_{phenyl}\cdots Cg_{phenyl\_a}$[b]	28.5	0.4
$Cg_{phenylene}\cdots Cg_{phenyl}$[b]	63.14(9)	53.6
$Cg_{phenylene}\cdots Cg_{phenyl\_a}$[b]	53.2	53.5

[a]Symmetry transformation used to generate equivalent atoms: _a 1 − *x*, −*y*, *z*. [b]Least-square planes, formed by the carbon atoms of the phenylene and phenyl rings, respectively

It was found that a Hirshfeld surface of **1**, calculated over d_{norm}, contains two symmetrical pairs of bright red spots, corresponding to donors and acceptors of the C–H···O intermolecular interactions (Fig. 5). The donors and the acceptors of these interactions can be evidenced as blue and red regions around the participating atoms on the Hirshfeld surface mapped over shape index corresponding to H···O contacts (Fig. 5). Moreover, no flat regions were observed on the Hirshfeld surface of **1**, mapped over curvedness, testifying to the absence of reasonable π···π interactions (Fig. 5).

It was also found that intermolecular H···H, H···C and H···O contacts, being about 55%, 35% and 9%, respectively, occupy almost the whole Hirshfeld surface of **1** (Table 3). The shortest H···H, H···C and H···O contacts are shown in the corresponding fingerprint plots at $d_e + d_i \approx 2.4$, 3.0 and 2.4 Å, respectively (Table 3). Notably, the H···C contacts are shown in the form of "wings" (Table 3), and are recognised as characteristic of C–H···π nature [49], while the H···O contacts are shown as a pair of spikes due to the formation of relatively strong C–H···O hydrogen bonds (Table 3). Furthermore, according to the Hirshfeld surface analysis only a very negligible proportion (1.0%) of the C···C contacts was found, indicating the absence of π···π stacking interactions (Table 3).

The H···C and H···O contacts in the structure of **1** are highly favoured since the corresponding enrichment ratios E_{HC} and E_{HO} are larger than unity and of 1.23 and 1.31, respectively (Table 3). This is explained by a relatively higher proportion of these contacts on the total Hirshfeld surface area over a corresponding proportion of random contacts R_{HC} and R_{HO}, respectively (Table 4). The H···H contacts are less favoured since the $E_{HH} = 0.92$ enrichment ratio is less than unity, which is related to the high enrichment of H···C and H···O contacts. The C···C contacts are significantly impoverished as evidenced from the corresponding enrichment ratio of 0.29.

Voids in the crystal structure of **1** (Fig. 6) were calculated using CrystalExplorer 17 [50]. It was found that the void volume is 198.93 $Å^3$ and the corresponding surface area is 537.83 $Å^2$. With the porosity, the calculated void volume of **1** is about 17%.

We have also calculated energy frameworks using CrystalExplorer 17 [50] to further analyse the crystal packing of **1**. A single-point molecular wavefunction at B3LYP/6-31G(d,p) was applied for a cluster of radius 3.8 Å to perform the energy calculation (Table 4, Fig. 7) [52]. The overall topology of the energy distributions in the crystal structure of **1** was studied through the energy framework. It was established that the structure is mainly characterized by the

Table 2 Hydrogen bond and C–H···π interaction lengths (Å) and angles (°) in the structure of **1**.[a]

D–H···A	*d*(D–H)	*d*(H···A)	*d*(D···A)	∠(DHA)
O1–H1···N1	0.82	1.85	2.5813(14)	148
C10–H10···O1[#1]	0.93	2.53	3.3516(19)	148
C–H(*I*)···Cg(*J*)[b]	*d*[H(*I*)···Cg(*J*)]	*d*[C···Cg(*J*)]	∠(CHCg)	*γ*
C5–H5···C_6H_5[#2]	2.99	3.6511(19)	129	11.71

[a]Symmetry transformations used to generate equivalent atoms: #1 1 − *x*, −*y*, 1 + *z*; #2 1/2 + *x*; 1/2 − *y*, 1 − *z*. [b]H(*I*)···Cg(*J*): distance of H to ring centroid; C···Cg(*J*): distance of C to ring centroid; ∠(CHCg): C–H···Cg angle; *γ*: angle between Cg(*J*)···H(*I*) vector and ring *J* normal

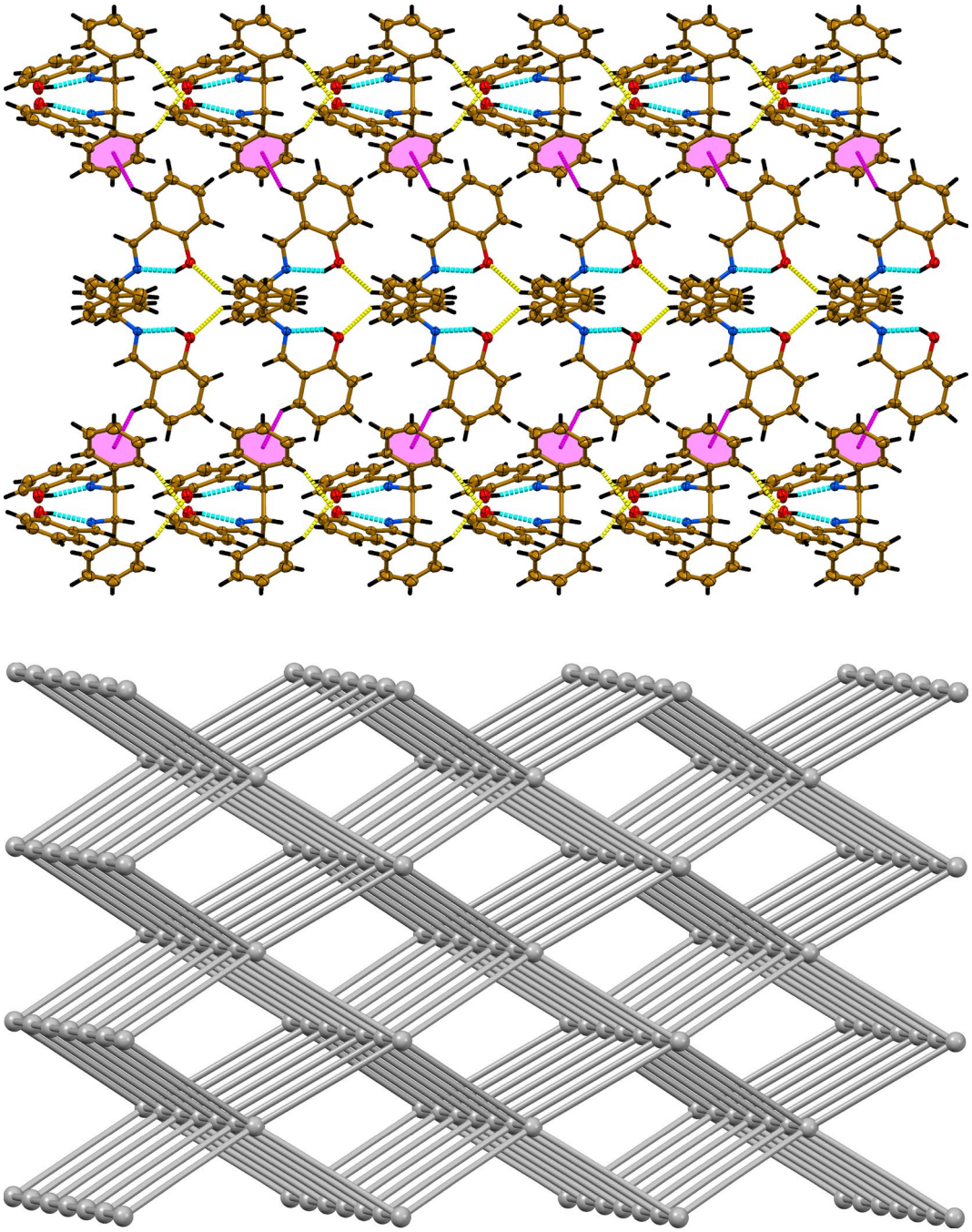

Fig. 4 (Top) Crystal packing of **1**, constructed from intermolecular C–H···O and C–H···π interactions. Colour code: H = black, C = gold, N = blue, O = red; N–H···O hydrogen bond = dashed cyan line, C–H···O interaction = dashed yellow line, C–H···π interaction = dashed magenta line. (bottom) A simplified network of **1**, constructed from intermolecular C–H···O and C–H···π interactions, with the uninodal 6-connected **pcu alpha-Po primitive cubic; 6/4/c1; sqc1** topology defined by the point symbol of $(4^{12}.6^3)$. Colour code: **1** = grey

dispersion energy framework followed by the less significant electrostatic energy framework contribution (Fig. 8).

We have further studied optical properties of **1** in different solvents to examine the influence of the solvent nature on the enol-imine and keto-enamine tautomerization. Particularly, we probed polar aprotic, namely THF, CH_2Cl_2 and CH_3CN, and a homologous series of polar protic solvents, namely MeOH, EtOH, *n*PrOH, *i*PrOH and *n*BuOH. It was recently established that the dipole moments for the keto-enamine tautomers are larger than those for the enol-imine tautomers

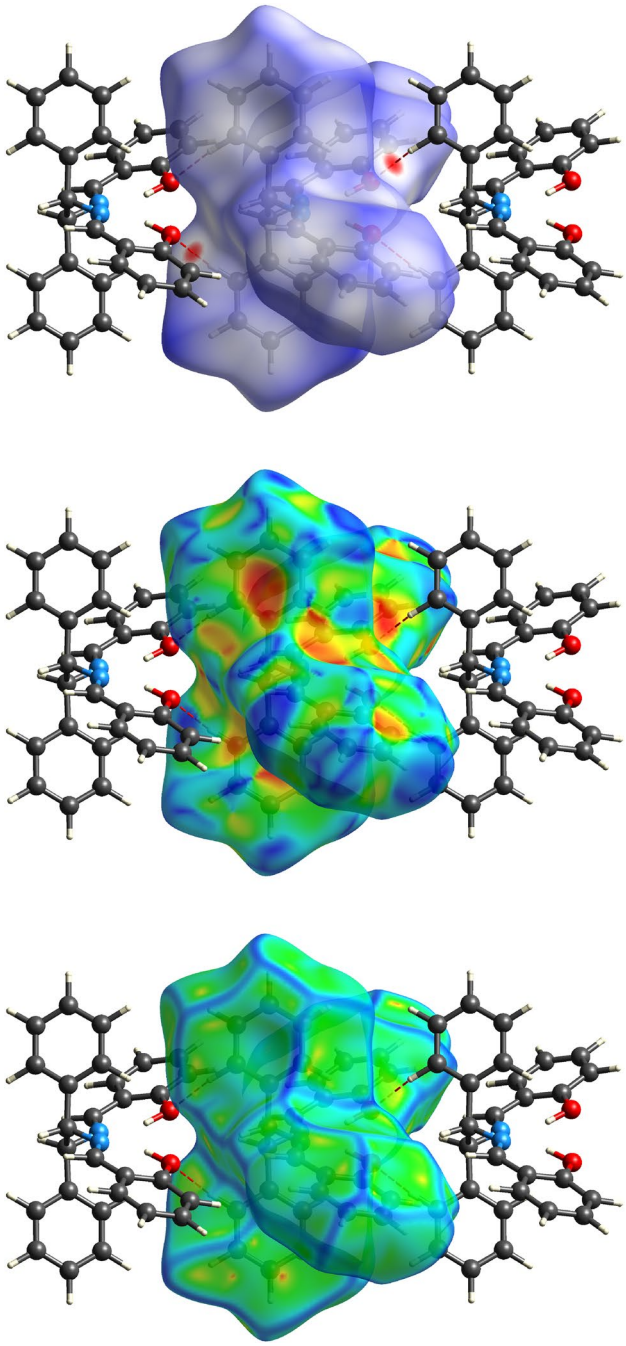

Fig. 5 Molecular Hirshfeld surfaces of **1** (top, middle, bottom denote normalized distance d_{norm}, shape index and curvedness, respectively)

[53, 54] that means that polar solvents shift the equilibrium towards and stabilize the former tautomer. This, in turn, is shown in the absorption spectrum by an additional band in the visible region at $\lambda_{max} \approx 400$ nm. Furthermore, in order to estimate the influence of a solvent onto a solute, the so-called solvatochromic comparison method is frequently applied [55, 56]. This method constitutes three main parameters, namely π*, *α* and *β* (Table 5). The parameter π* measures *the ability of the solvent to stabilize a charge or a dipole by virtue of its dielectric effect*. The parameter *α describes the ability of the solvent to donate a proton in a solvent-to-solute hydrogen bond*, while the parameter *β provides a measure of the solvent's ability to accept a proton (donate an electron pair) in a solute-to-solvent hydrogen bond*.

The absorption spectra of **1** in THF, CH_2Cl_2 and CH_3CN are very similar and each exhibit three intense bands exclusively in the UV region centred at about 220–230, 255–260 and 315–320 nm (Fig. 9). The two high-energy bands correspond to the intramolecular $\pi \rightarrow \pi^*$ transitions of the aromatic and imine moieties, while the low-energy band corresponds to the $n \rightarrow \pi^*$ transition of the imine fragments. The absorption spectra of **1** in EtOH, *n*PrOH, *i*PrOH and *n*BuOH, besides the same three intense bands in the UV region, contain an additional low intense band in the visible region centred at about 410 nm (Fig. 9), corresponding to the *cis*-keto-enamine tautomer. The most striking finding is that the absorption spectrum of **1** in MeOH, exhibiting the same four bands as in the spectra of **1** in other alcohols, contains an additional intense shoulder at about 350 nm (Fig. 9).

We have next studied emission properties of **1** in the applied solvents. It was established that **1** is emissive in MeOH at $\lambda_{exc} = 350$ nm (Fig. 10). The emission spectrum exhibits one broad band centred at 438 nm. Comparison of the excitation and UV–vis spectra of **1** in MeOH allowed to conclude that the emission bands arise from the emission of the enol-imine* form. The resulting blue colour of the emission of the solution of **1** in MeOH was quantified with the chromaticity coordinates (0.15, 0.06).

We have further applied the density functional theory (DFT) calculations to examine fine features of **1**. The ground state geometry of **1** was first fully optimized at the B3LYP/6–311 ++ G(d,p) [38–40] level. It was established that the calculated values of bond lengths, bond angles and dihedral angles are in good agreement with the values obtained from single-crystal X-ray diffraction (Table 1). The observed differences between the calculated and experimental geometrical parameters are obviously explained by the fact that the DFT computations were performed in the gas phase.

According to the DFT calculations, the dipole moment of the fully optimized ground state geometry of **1** is 3.722719 Debye, while the energies of the frontier molecular orbitals are −0.22825 and −0.06403 eV for the highest occupied molecular orbital (HOMO) and lowest lying unoccupied molecular orbital (LUMO), respectively (Table 6). Both orbitals are delocalized over the (*ortho*-OH-C_6H_4–CH=N–CH–)$_2$ fragment except the imine CH group for HOMO and the 5-CH group of the C_6H_4 fragment for LUMO (Fig. 11). Delocalization of LUMO+1 is similar to LUMO with some minor differences, while the HOMO–1

Table 3 (Top) 2D and decomposed 2D fingerprint plots of observed contacts for **1**. (bottom) Hirshfeld contact surfaces and derived "random contacts" and "enrichment ratios" for **1**

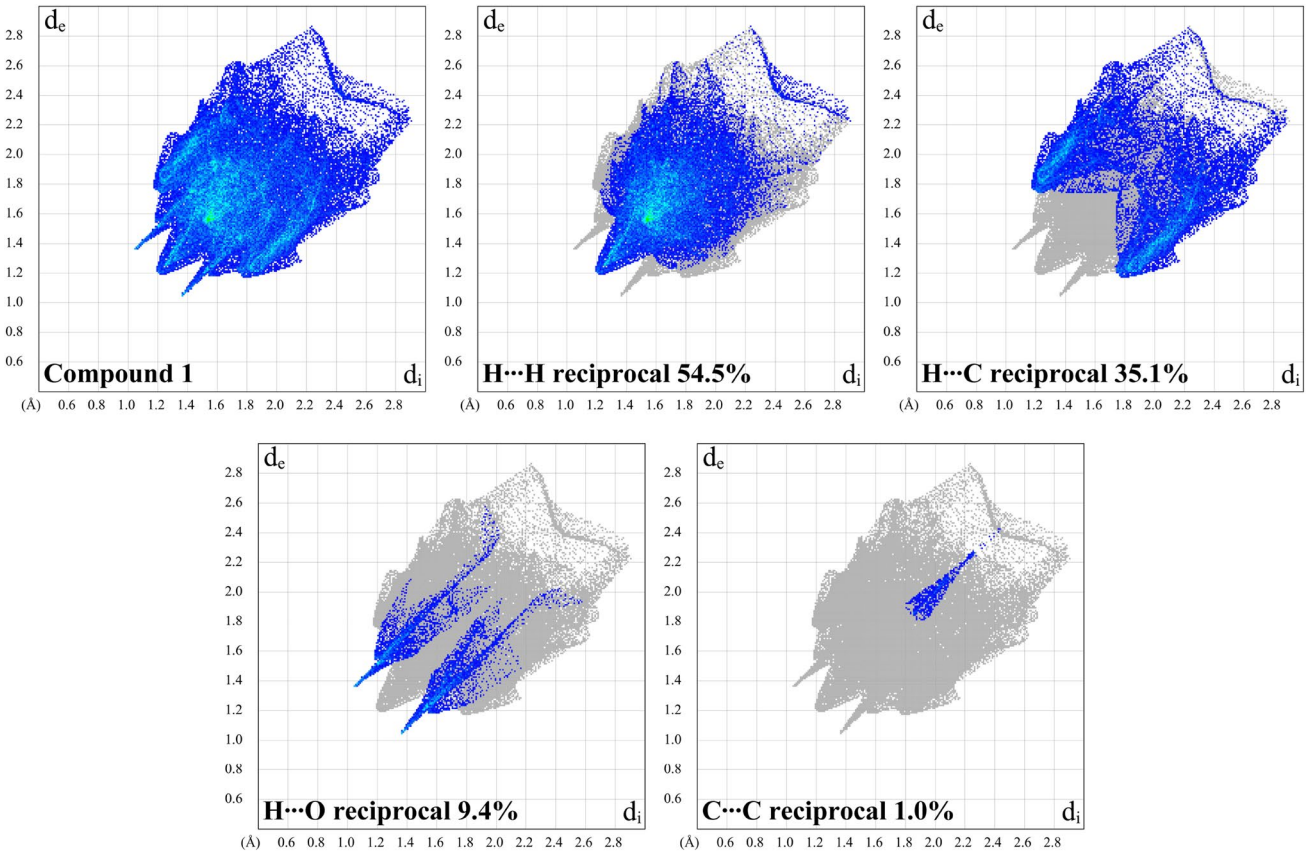

	H	C	N	O
Contacts (*C*, %)[a]				
H	54.5	–	–	–
C	35.1	1.0	–	–
N	0.0	0.0	0.0	–
O	9.4	0.0	0.0	0.0
Surface (*S*, %)				
	76.8	18.6	0.0	4.7
Random contacts (*R*, %)				
H	59.0	–	–	–
C	28.6	3.5	–	–
N	0.0	0.0	0.0	–
O	7.2	1.7	0.0	0.2
Enrichment (*E*)[b]				
H	0.92	–	–	–
C	1.23	0.29	–	–
N	–	–	–	–
O	1.31	0.0	–	–

[a]Values are obtained from CrystalExplorer 17 [50]. [b]The "enrichment ratios" were not computed when the "random contacts" were lower than 0.9%, as they are not meaningful [51]

Table 4 Interaction energies (kJ/mol) calculated for the crystal structure of **1**.[a]

	N	symmetry operation	*R*	electron density	E_{ele} [b]	E_{pol} [b]	E_{dis} [b]	E_{rep} [b]	E_{tot} [b]
	4	$x+1/2, -y+1/2, -z$	10.44	B3LYP/6-31G(d,p)	−3.6	−0.8	−21.6	8.9	−17.7
	4	x, y, z	12.37	B3LYP/6-31G(d,p)	−1.3	−0.2	−9.2	3.8	−7.3
	4	$x+1/2, -y+1/2, -z$	10.09	B3LYP/6-31G(d,p)	−3.5	−1.0	−23.0	10.6	−17.8
	2	x, y, z	10.21	B3LYP/6-31G(d,p)	−4.6	−1.3	−34.6	17.7	−24.9
	2	x, y, z	6.99	B3LYP/6-31G(d,p)	−19.9	−6.8	−47.0	35.5	−45.2

[a]*N* is the number of molecules with an *R* molecular centroid-to-centroid distance (Å); colour codes in the first column are referenced to Fig. 7. [b]E_{ele} is the electrostatic energy, E_{pol} is the polarization energy, E_{dis} is the dispersion energy, E_{rep} is the exchange-repulsion energy, *k* values are scale factors; $E_{tot}=k_{ele}\times E_{ele}+k_{pol}\times E_{pol}+k_{dis}\times E_{dis}+k_{rep}\times E_{rep}=1.057\times E_{ele}+0.740\times E_{pol}+0.871\times E_{dis}+0.618\times E_{rep}$ [52]

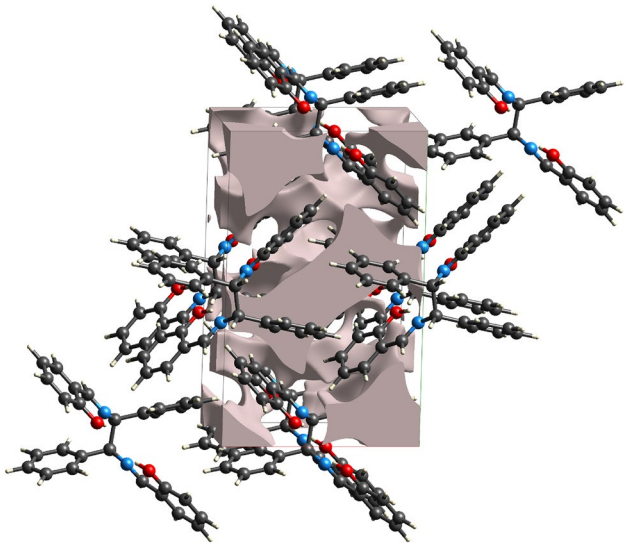

Fig. 6 Void plot for **1** (results under 0.002 a.u. isovalue)

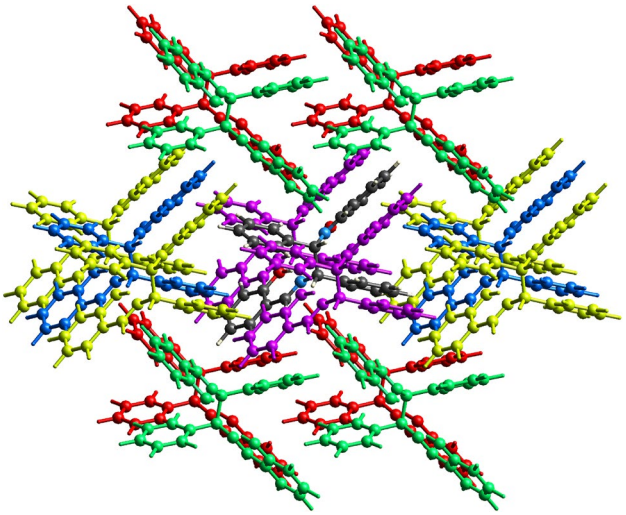

Fig. 7 Colour-coded interaction mapping within 3.8 Å of the centring molecule in the crystal structure of **1**, calculated from a single-point molecular wavefunction at B3LYP/6-31G(d,p)

is delocalized over two *ortho*-OH-C_6H_4 fragments and both imine nitrogen atoms (Fig. 11). HOMO–2, LUMO+2 and LUMO+3 are spread over the $(CH{=}N{-}CH(C_6H_5){-})_2$, $(N{-}CH(C_6H_5){-})_2$ and $(CH(C_6H_5){-})_2$ fragments, respectively, while HOMO–3 is spread over the non-hydrogen atoms of the whole molecule except the two (HO)C-carbon atoms and two *para*-C-carbons of the phenyl fragments (Fig. 11).

The HOMO and LUMO values also establish the ionization potential (*I*) and the electron affinity (A) value of the molecule, respectively, according to the relation: $I=-E_{HOMO}$ and $A=-E_{LUMO}$ (Table 6) [57]. These parameters are of importance, and *I* and *A* determine the electron donating ability and the ability to accept an electron, respectively. Particularly, lower values of *I* are responsible for the better donation of an electron, while higher values of *A* indicate a better ability to accept electrons. Both the *I* and *A* values for **1** are relatively low (Table 6), indicating that **1** is a good electron donor.

We have also established values of the so-called global chemical reactivity descriptors, which are derived from the HOMO-LUMO energy gap, to estimate the relative reactivity of a molecule of **1**. The value of chemical potential (μ) for **1** is −0.14614 eV, indicating the poor electron accepting ability and the strong donating ability, which is further supported with a low value of electronegativity, χ (Table 6). The chemical hardness (η) describes the resistance towards deformation/polarization of the electron cloud of the molecule upon a chemical reaction, while softness (*S*) is a reverse of chemical hardness [57]. Compound **1** is

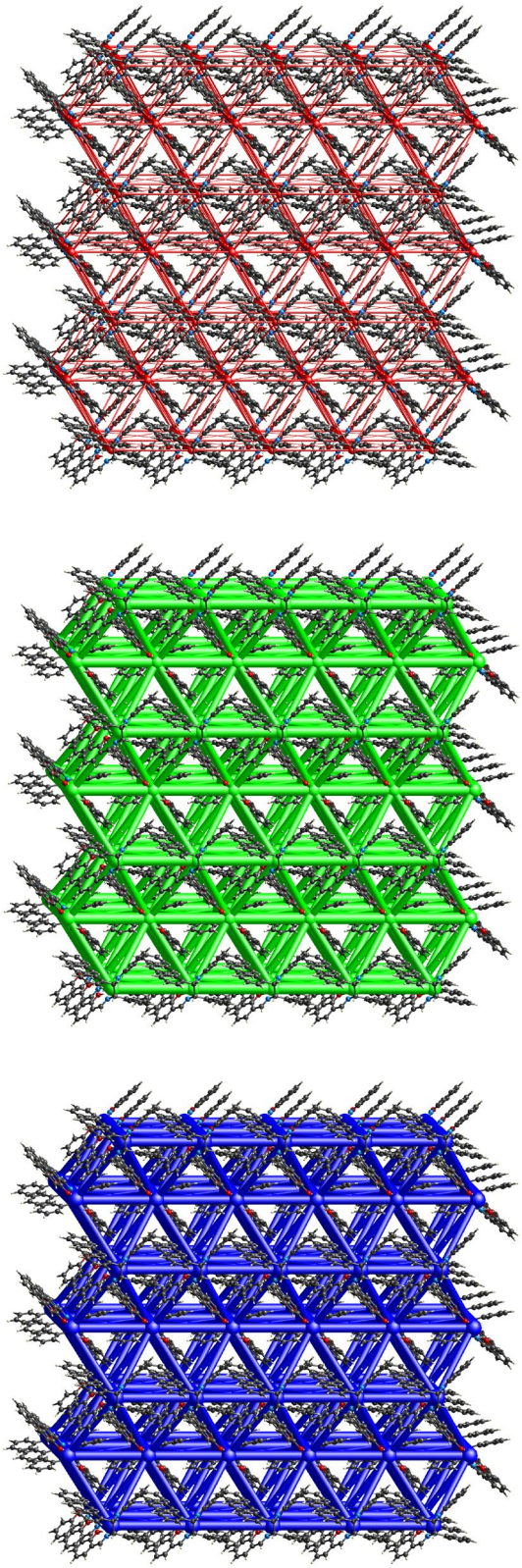

Fig. 8 Energy frameworks calculated for the crystal structure of **1**, showing the (top) electrostatic potential force, (moddle) dispersion force and (bottom) total energy diagrams. The cylindrical radii are proportional to the relative strength of the corresponding energies and they were adjusted to the same scale factor of 250 within 5×3×2 unit cells

Table 5 Solvatochromic parameters of the applied solvents [55, 56]

Solvent	π*	α	β
THF	0.58	0.00	0.55
CH_2Cl_2	0.82	0.30	0.00
CH_3CN	0.75	0.19	0.31
*n*BuOH	0.47	0.79	0.88
*i*PrOH	0.48	0.76	0.95
*n*PrOH	0.52	0.78	0.90
EtOH	0.54	0.83	0.77
MeOH	0.60	0.93	0.62

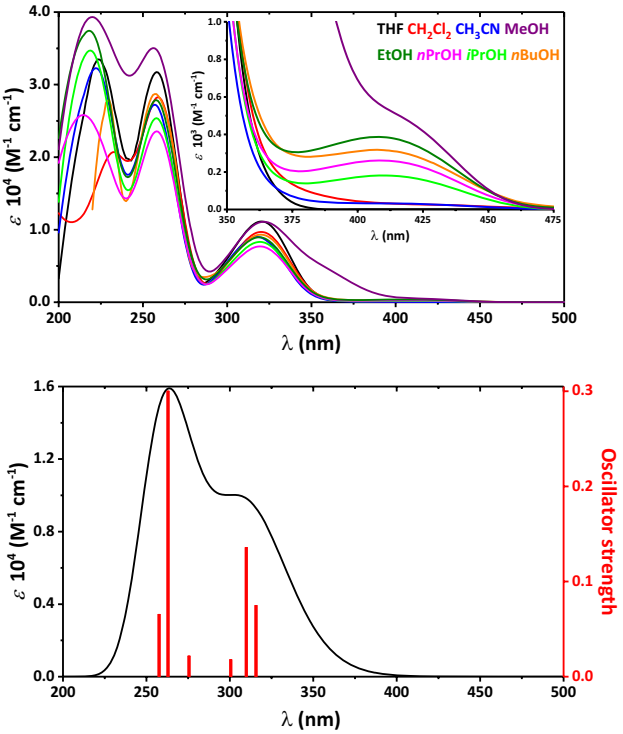

Fig. 9 (top) Experimental UV–vis spectra of **1** in different solvents (concentration = 10^{-4} M). (bottom) The calculated UV–vis spectrum of the ground state of **1**, obtained by using the TD-DFT/B3LYP/6–311 ++ G(d,p) method

characterized by a low value of η (0.08211 eV) and a high value of S (6.08936 eV^{-1}), respectively, indicating that **1** exhibits a remarkable tendency to exchange its electron cloud with surrounding environment. The next descriptor, namely electrophilicity index (ω), describes the energy of stabilization to accept electrons [57]. The ω value for **1** was found to be 0.13005 eV. This value is remarkably low, indicating the strong nucleophilic nature of **1**. Finally, compound

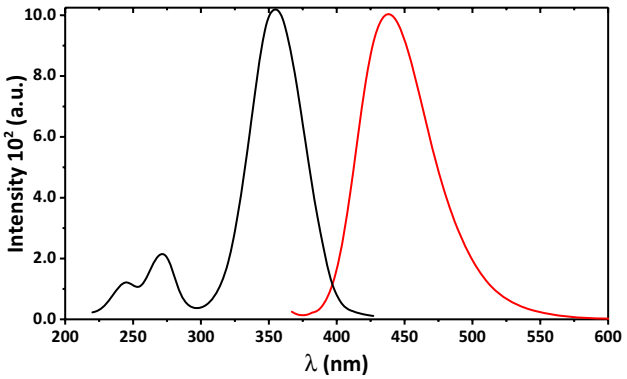

Fig. 10 Emission (red) and excitation (black) spectra of **1** in MeOH (concentration = 10^{-6} M; λ_{exc} = 350 nm, λ_{em} = 435 nm)

1 can accept about 1.78 electrons as evidenced from the ΔN_{max} value (Table 6).

We have also applied the molecular electrostatic potential (MEP) analysis towards **1** to probe the electrophilic and nucleophilic sites in a molecule. The MEP surface of **1**, generated from the fully optimized ground state geometry obtained by using the B3LYP/6–311 ++ G(d,p) method, exhibits the electrostatic potential regions denoted by different colour code, where the red and blue colours correspond to electron rich (nucleophilic) and electron deficient (electrophilic) regions, respectively (Fig. 12). In the MEP surface of **1**, the most negative potentials are located on both hydroxyl oxygen atoms, indicating nucleophilic sites with the strongest attraction for electrophilic attack. The most positive potentials, coloured as blue regions, are located on the hydrogen atoms of the imine groups, 6-H-atoms of the phenylene rings, hydrogen atoms of the bridging CH–CH fragment and one half of the hydrogen atoms of the phenyl rings (Fig. 12), indicating electrophilic sites being the most attractive for nucleophilic attacks.

The absorption spectrum of the fully optimized ground state geometry obtained by using the B3LYP/6–311 ++ G(d,p) method was simulated at the TD-DFT/B3LYP/6–311 ++ G(d,p) level. The calculated UV–vis spectrum exhibits an intense absorption band centred at about 263 nm accompanied with a shoulder at about 310 nm (Fig. 9). Each absorption band comprises three transitions at 257–276 nm and 300–316 nm, respectively, with HOMO–3, HOMO–2, HOMO–1, HOMO, LUMO and LUMO+1 being the main contributors. (Fig. 9, Table 7). In general, the calculated UV–vis spectrum is similar to the experimental ones recorded in THF, CH_2Cl_2 and CH_3CN (Fig. 9).

Table 6 Total energy, dipole moment, frontier molecular HOMO and LUMO orbitals, gap value and descriptors for **1** in gas phase, obtained by using the B3LYP/6–311 ++ G(d,p) method

Dipole moment (Debye)	3.722719
E_{HOMO} (eV)	−0.22825
E_{LUMO} (eV)	−0.06403
$\Delta E_{LUMO\ -\ HOMO} = E_{LUMO} - E_{HOMO}$ (eV)	0.16422
Ionization energy, $I = -E_{HOMO}$ (eV)	0.22825
Electron affinity, $A = -E_{LUMO}$ (eV)	0.06403
Electronegativity, $\chi = (I+A)/2$ (eV)	0.14614
Chemical potential, $\mu = -\chi$ (eV)	−0.14614
Global chemical hardness, $\eta = (I - A)/2$ (eV)	0.08211
Global chemical softness, $S = 1/(2\eta)$ (eV^{-1})	6.08936
Global electrophilicity index, $\omega = \mu^2/(2\eta)$ (eV)	0.13005
Global nucleophilicity index, $E = \mu \times \eta$ (eV^2)	−0.01200
Maximum additional electric charge, $\Delta N_{max} = -\mu/\eta$	1.77981

To evaluate a potential antifungal activity of **1** we have further applied in silico molecular docking studies against cytochrome P450 14 alpha-sterol demethylase (CYP51). The target enzyme was obtained from the Protein Data Bank (PDB) [58]. Using the AutoDock MGL Tools package [59], the heteroatoms and water molecules were removed from the protein and polar hydrogens were added. Finally, the prepared enzyme was converted into the pdbqt format for docking process with AutoDock Vina [60]. The binding free energy of resulting complex was calculated by docking with active site residues with grid coordinates ($x = -17.295$, $y = -2.725$, $z = 66.753$). Interactions of the docked complex were analysed using Discovery Studio visualizer [61].

To validate the docking procedure, the native ligand fluconazole was redocked with the enzyme. The docking results revealed a higher docking energy for the complex with **1** (−9.2 kcal/mol) than with fluconazole (−8.6 kcal/mol). The complex with **1** is stabilized by trifurcated conventional hydrogen bonds (ARG96), one electrostatic π-cation (ARG96), one hydrophobic π-sigma interaction (TYR76), and two π-sulphur bonds (MET79) with the active residues mentioned in parenthesis (Fig. 13). The presence of various non-covalent interactions in the complex with **1** leads to superior binding affinity and antifungal nature of **1** over the native ligand fluconazole, which is a popular antifungal drug. Hence, **1** may be considered as an effective inhibitor of cytochrome P450 14 alpha-sterol demethylase (CYP51) and an antifungal drug.

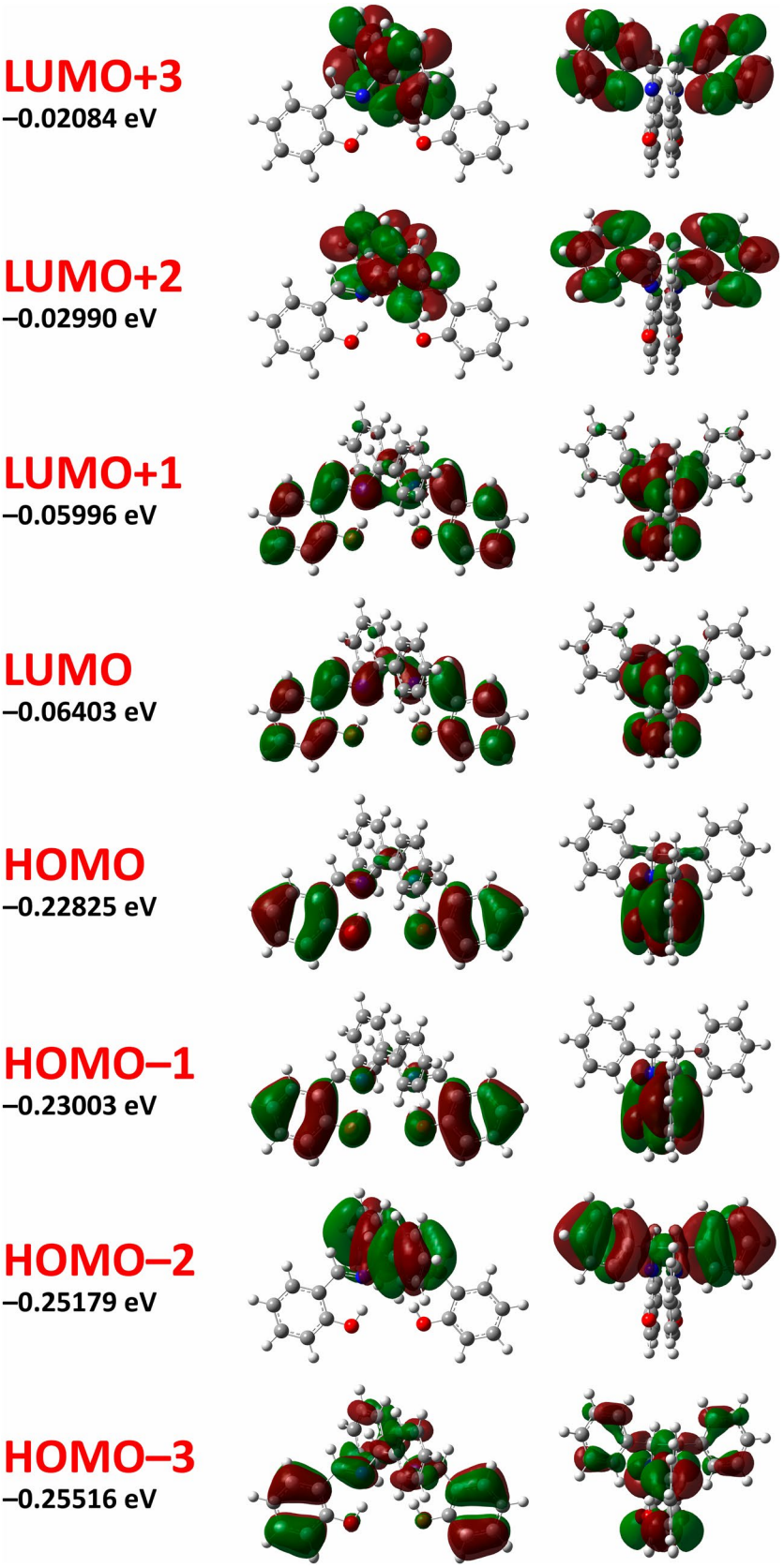

Fig. 11 Energy levels, and (left) front and (right) side views on the electronic isosurfaces of the selected molecular orbitals of the ground state of **1**, obtained by using the B3LYP/6–311 + + G(d,p) method

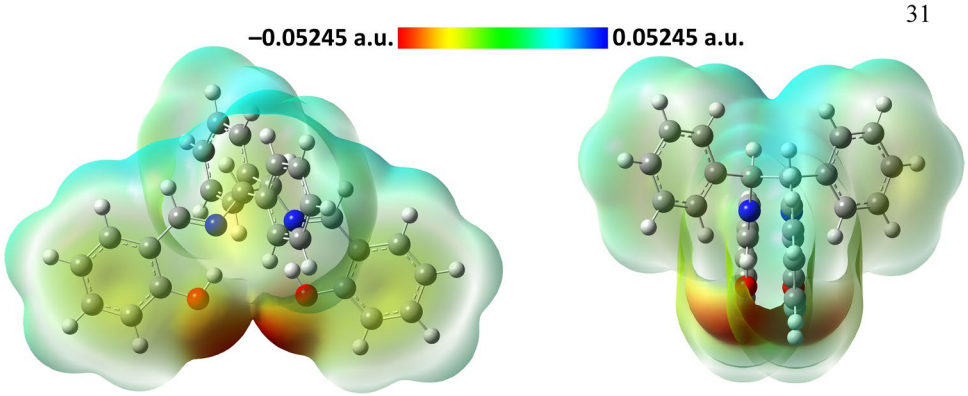

Fig. 12 (left) Front and (right (side) views of the molecular electrostatic potential surface of **1**, obtained by using the B3LYP/6–311 + + G(d,p) method

Table 7 Values for the calculated UV–vis spectrum of the ground state of **1** (Fig. 13), obtained by using the TD-DFT/B3LYP/6–311 + + G(d,p) method

λ_{max} (nm)	Oscillator strength	Transitions
257.6	0.0655	HOMO–8 → LUMO (20.5%)
		HOMO–4 → LUMO (61.4%)
262.9	0.3002	HOMO–3 → LUMO (82.4%)
275.5	0.0217	HOMO–2 → LUMO (97.7%)
300.5	0.0178	HOMO–1 → LUMO (21.2%)
		HOMO → LUMO+1 (77.6%)
309.8	0.1358	HOMO–1 → LUMO (75.0%)
		HOMO → LUMO+1 (18.4%)
315.7	0.0747	HOMO–1 → LUMO+1 (13.3%)
		HOMO → LUMO (83.0%)

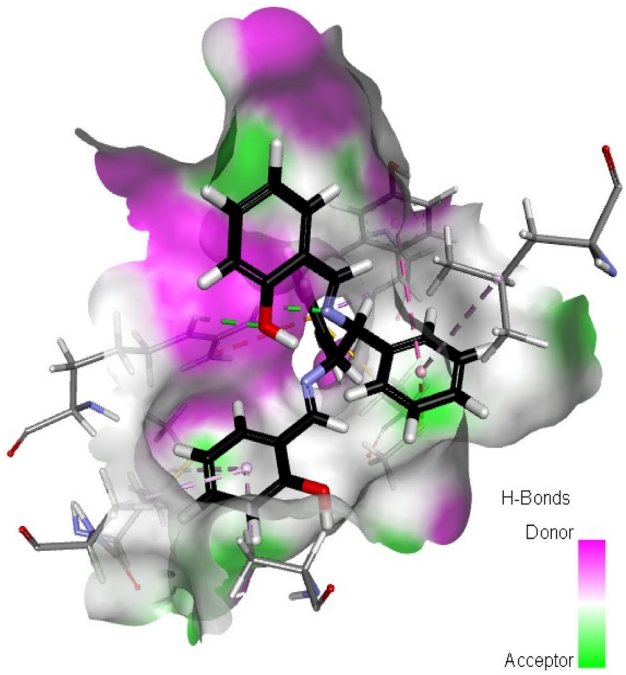

Fig. 13 Docking interactions of **1** and cytochrome P450 14 alpha-sterol demethylase (CYP51) active site residues

Conclusions

In summary, we report detailed structural studies as well as photophysical properties of a chiral (1*R*,2*R*)-*N*,*N*′-*bis*-(salicylidene)-1,2-diphenyl-1,2-ethanediamine Schiff base dye (**1**), obtained by the condensation reaction of (1*R*,2*R*)-1,2-diphenyl-1,2-ethanediamine with two equivalents of salicylaldehyde in ethanol.

Single crystal X-ray diffraction revealed that the molecule of **1** lies on a crystallographic two-fold axis; thus, the asymmetric unit comprises one half-molecule exhibiting an enol-imine tautomer, stabilized by two intramolecular O–H···N hydrogen bonds. The structure of **1** is further stabilized by intermolecular C–H···O interactions, yielding a 1D supramolecular chain, which, in turn, are further interlinked through intermolecular C–H···π intercations. As a result of intermolecular interactions, molecules of **1** are packed into a 3D supramolecular framework, yielding a **pcu alpha-Po primitive cubic; 6/4/c1; sqc1** topology defined by the point symbol of (4^{12}·6^3).

According to the Hirshfeld surface analysis data, favoured intermolecular H···H, H···C and H···O contacts in the structure of **1** are responsible for the overall crystal packing. Energy frameworks have been calculated to additionally analyse the overall crystal packing of **1**. It was established that the structure is mainly characterized by the dispersion energy framework followed by the less significant electrostatic energy framework contribution.

The absorption spectra of **1** in THF, CH_2Cl_2 and CH_3CN are very similar and each exhibit three intense bands exclusively in the UV region centred at about 220–230, 255–260 and 315–320 nm. The absorption spectra of **1** in EtOH, *n*PrOH, *i*PrOH and *n*BuOH, besides the same three intense bands in the UV region, contain an additional low intense band in the visible region centred at about 410 nm, corresponding to the *cis*-keto-enamine tautomer. Notably, the absorption spectrum of **1** in MeOH, exhibiting the same four bands as in the spectra of **1** in other alcohols, contains an additional intense shoulder at about 350 nm. The emission

spectrum of **1** in MeOH contains a broad band at 438 nm, arising from the emission of the enol-imine* form. The resulting blue colour of the emission of the solution of **1** in MeOH was quantified with the chromaticity coordinates (0.15, 0.06).

According to the DFT calculation results it was established that **1** is a good electron donor with a strong nucleophilic nature. The nucleophilic sites with the strongest attraction for electrophilic attack are located on both hydroxyl oxygen atoms.

In silico molecular docking studies were carried out for **1** with cytochrome P450 14 alpha-sterol demethylase (CYP51) and the results revealed that **1** has promising binding affinity over fluconazole.

Author contributions A. A. S. involved in conducting research and partial analysis of results; A. N. G. involved in conducting research and partial analysis of results; T. M. B. involved in planning research, analysis results, and preparing a manuscript; L. E. A. involved in conducting research and partial analysis of results; M. G. B. involved in planning research, analysis results, and preparing a manuscript; R. C. involved in conducting molecular docking and analysis of results; D. A. S. involved in planning research, analysis results, and preparing a manuscript.

Funding Not applicable.

Availability of data and materials Not applicable.

Declarations

Consent to participate Not applicable.

Consent to publish Not applicable.

Competing interests The authors declare that they have no conflicts of interest in this work.

Ethical approval Not applicable.

References

1. H. Schiff, Eur. J. Org. Chem. **131**, 118–119 (1864)
2. IUPAC. Compendium of Chemical Terminology, 2nd ed. (the "Gold Book"). Compiled by A.D. McNaught, A. Wilkinson. Blackwell Scientific Publications, Oxford (1997)
3. https://goldbook.iupac.org/terms/view/A00357
4. S. Yamada, Coord. Chem. Rev. **190–192**, 537–555 (1999)
5. P.G. Cozzi, Chem. Soc. Rev. **33**, 410–421 (2004)
6. C. Baleizão, H. Garcia, Chem. Rev. **106**, 3987–4043 (2006)
7. A. Decortes, A.M. Castilla, A.W. Kleij, Angew. Chem. Int. Ed. **49**, 9822–9837 (2010)
8. S. Shaw, J.D. White, Chem. Rev. **119**, 9381–9426 (2019)
9. W. Zhang, J.L. Loebach, S.R. Wilson, E.N. Jacobsen, J. Am. Chem. Soc. **112**, 2801–2803 (1990)
10. E.N. Jacobsen, W. Zhang, A.R. Muci, J.R. Ecker, L. Deng, J. Am. Chem. Soc. **113**, 7063–7064 (1991)
11. W. Dabelstein, A. Reglitzky, A. Schütze, K. Reders, A. Brunner, *Ullmann's Encyclopedia of Industrial Chemistry* (Wiley, Weinheim, 2016).
12. H.C. Aspinall, Chem. Rev. **102**, 1807–1850 (2002)
13. J. Crassous, Chem. Soc. Rev. **38**, 830–845 (2009)
14. M. Liu, L. Zhang, T. Wang, Chem. Rev. **115**, 7304–7397 (2015)
15. E. Hadjoudis, M. Vitterakis, I. Moustakali, I. Mavridis, Tetrahedron **43**, 1345–1360 (1987)
16. E. Hadjoudis, I.M. Mavridis, Chem. Soc. Rev. **33**, 579–588 (2004)
17. K. Amimoto, T. Kawato, J. Photochem. Photobiol. C **6**, 207–226 (2005)
18. T. Haneda, M. Kawano, T. Kojima, M. Fujita, Angew. Chem. Int. Ed. **46**, 6643–6645 (2007)
19. A. Filarowski, A. Koll, L. Sobczyk, Curr. Org. Chem. **13**, 172–193 (2009)
20. V. Bertolasi, P. Gilli, G. Gilli, Curr. Org. Chem. **13**, 250–268 (2009)
21. E. Hadjoudis, S.D. Chatziefthimiou, I.M. Mavridis, Curr. Org. Chem. **13**, 269–286 (2009)
22. V.I. Minkin, A.V. Tsukanov, A.D. Dubonosov, V.A. Bren, J. Mol. Struct. **998**, 179–191 (2011)
23. Y. Inokuma, M. Kawano, M. Fujita, Nat. Chem. **3**, 349–358 (2011)
24. K.T. Mahmudov, A.J.L. Pombeiro, Chem. Eur. J. **22**, 16356–16398 (2016)
25. D.A. Safin, K. Robeyns, Y. Garcia, CrystEngComm **14**, 5523–5529 (2012)
26. D.A. Safin, K. Robeyns, Y. Garcia, RSC Adv. **2**, 11379–11388 (2012)
27. D.A. Safin, Y. Garcia, RSC Adv. **14**, 6466–6471 (2013)
28. D.A. Safin, M. Bolte, Y. Garcia, CrystEngComm **16**, 5524–5526 (2014)
29. D.A. Safin, M.G. Babashkina, K. Robeyns, M. Bolte, Y. Garcia, CrystEngComm **16**, 7053–7061 (2014)
30. D.A. Safin, M. Bolte, Y. Garcia, CrystEngComm **16**, 8786–8793 (2014)
31. D.A. Safin, M.G. Babashkina, K. Robeyns, Y. Garcia, RSC Adv. **16**, 53669–53678 (2016)
32. D.A. Safin, K. Robeyns, M.G. Babashkina, Y. Filinchuk, A. Rotaru, C. Jureschi, M.P. Mitoraj, J. Hooper, M. Brela, Y. Garcia, CrystEngComm **16**, 7249–7259 (2016)
33. D.A. Safin, K. Robeyns, Y. Garcia, CrystEngComm **18**, 7284–7296 (2016)
34. A.A. Shiryaev, T.M. Burkhanova, G. Mahmoudi, M.G. Babashkina, D.A. Safin, J. Lumin. **226**, 117454 (2020)
35. D.S. Shapenova, A.A. Shiryaev, M. Bolte, M. Kukułka, D.W. Szczepanik, J. Hooper, M.G. Babashkina, G. Mahmoudi, M.P. Mitoraj, D.A. Safin, Chem. Eur. J. **26**, 12987–12995 (2020)
36. R. Dennington, T.A. Keith, J.M. Millam, GaussView, Version 6.0, Semichem Inc., Shawnee Mission, KS, 2016
37. M.J. Frisch, G.W. Trucks, H.B. Schlegel, G.E. Scuseria, M.A. Robb, J.R. Cheeseman, G. Scalmani, V. Barone, B. Mennucci, G.A. Petersson, H. Nakatsuji, M. Caricato, X. Li, H.P. Hratchian, A.F. Izmaylov, J. Bloino, G. Zheng, J.L. Sonnenberg, M. Hada, M. Ehara, K. Toyota, R. Fukuda, J. Hasegawa, M. Ishida, T. Nakajima, Y. Honda, O. Kitao, H. Nakai, T. Vreven, J.A. Montgomery Jr., J.E. Peralta, F. Ogliaro, M. Bearpark, J.J. Heyd, E. Brothers, K.N. Kudin, V.N. Staroverov, T. Keith, R. Kobayashi, J. Normand, K. Raghavachari, A. Rendell, J.C. Burant, S.S. Iyengar, J. Tomasi, M. Cossi, N. Rega, J.M. Millam, M. Klene, J.E. Knox, J.B. Cross, V. Bakken, C. Adamo, J. Jaramillo, R. Gomperts, R.E. Stratmann, O. Yazyev, A.J. Austin, R. Cammi, C. Pomelli, J.W. Ochterski, R.L. Martin, K. Morokuma, V.G. Zakrzewski, G.A. Voth, P. Salvador, J.J. Dannenberg, S. Dapprich, A.D. Daniels, O. Farkas, J.B. Foresman, J.V. Ortiz, J. Cioslowski, D.J. Fox, Gaussian 09, Revision D.01 (2013)

38. R. Krishnan, J.S. Binkley, R. Seeger, J.A. Pople, J. Chem. Phys. **72**, 650–654 (1980)
39. A.D. Becke, J. Chem. Phys. **98**, 5648–5652 (1993)
40. M.J. Frisch, J.A. Pople, J.S. Binkley, J. Chem. Phys. **80**, 3265–3269 (1984)
41. C.R. Groom, I.J. Bruno, M.P. Lightfoot, S.C. Ward, Acta Crystallogr. B **72**, 171–179 (2016)
42. T. Wu, CSD Communication (2017)
43. T.M. Krygowski, K. Woźniak, R. Anulewicz, D. Pawlak, W. Kolodziejski, E. Grech, A. Szady, J. Phys. Chem. A **101**, 9399–9404 (1997)
44. P.M. Dominiak, E. Grech, G. Barr, S. Teat, P. Mallinson, K. Woźniak, Chem. Eur. J. **9**, 963–970 (2003)
45. G.M. Mercier, K. Robeyns, T. Leyssens, Cryst. Growth Des. **16**, 3198–3205 (2016)
46. R.F. Martínez, E. Matamoros, P. Cintas, J.C. Palacios, J. Org. Chem. **85**, 5838–5862 (2020)
47. V.A. Blatov, A.P. Shevchenko, D.M. Proserpio, Cryst. Growth Des. **14**, 3576–3586 (2014)
48. M.A. Spackman, D. Jayatilaka, CrystEngComm **11**, 19–32 (2009)
49. M.A. Spackman, J.J. McKinnon, CrystEngComm **4**, 378–392 (2002)
50. M.J. Turner, J.J. McKinnon, S.K. Wolff, D.J. Grimwood, P.R. Spackman, D. Jayatilaka, M.A. Spackman, CrystalExplorer17, University of Western Australia, http://hirshfeldsurface.net (2017)
51. C. Jelsch, K. Ejsmont, L. Huder, IUCrJ **1**, 119–128 (2014)
52. C.F. Mackenzie, P.R. Spackman, D. Jayatilaka, M.A. Spackman, IUCrJ **4**, 575–587 (2017)
53. S.H. Alarcón, A.C. Olivieri, D. Sanz, R.M. Claramunt, J. Elguero, J. Mol. Struct. **705**, 1–9 (2004)
54. P.I. Nagy, W.M.F. Fabian, J. Phys. Chem. B **110**, 25026–25032 (2006)
55. M.J. Kamlet, J.-L.M. Abboud, M.H. Abraham, R.W. Taft, J. Org. Chem. **48**, 2877–2887 (1983)
56. Y. Marcus, J. Solut. Chem. **20**, 929–944 (1991)
57. P. Geerlings, F. De Proft, W. Langenaeker, Chem. Rev. **103**, 1793–1873 (2003)
58. https://www.rcsb.org/structure/1EA1
59. G.M. Morris, R. Huey, W. Lindstrom, M.F. Sanner, R.K. Belew, D.S. Goodsell, A.J. Olson, J. Comp. Chem. **16**, 2785–2791 (2009)
60. O. Trott, A.J. Olson, J. Comput. Chem. **31**, 455–461 (2010)
61. Discovery Studio 2015: Dassault Systemes BIOVIA, Discovery Studio Modelling Environment, Release 4.5, San Diego: Dassault Systemes